Applied Surface Science 637 (2023) 157901

Contents lists available at ScienceDirect

Applied Surface Science

journal homepage: www.elsevier.com/locate/apsusc

Full Length Article

Surface defect passivation of All-Inorganic $CsPbI_2Br$ perovskites via fluorinated ionic liquid for efficient Outdoor/Indoor photovoltaics processed in ambient air

Jitendra Bahadur [a], SungWon Cho [b], Padmini Pandey [a], Jun Ryu [b], Saemon Yoon [b], Dong-Gun Lee [b], Jun Tae Song [c,d], Jung Sang Cho [e,*], Dong-Won Kang [a,b,*]

[a] Department of Energy Systems Engineering, Chung-Ang University, Seoul 06974, Republic of Korea
[b] Department of Smart Cities, Chung-Ang University, Seoul 06974, Republic of Korea
[c] Department of Applied Chemistry, Faculty of Engineering, Kyushu University, Motooka 744, Nishi-ku, Fukuoka 819-0395, Japan
[d] International Institute for Carbon-Neutral Energy Research (WPI-I2CNER), Kyushu University, Motooka 744, Nishi-ku, Fukuoka 819-0395, Japan
[e] Department of Engineering Chemistry, Chungbuk National University, Chungbuk 361-763, Republic of Korea

ARTICLE INFO

Keywords:
Inorganic perovskite solar cells
Surface passivation strategy
3-(Trifluoromethyl) benzylamine
Outdoor/Indoor photovoltaics

ABSTRACT

All-inorganic α-$CsPbI_2Br$ perovskite has garnered considerable interest due to its optical bandgap (~1.92 eV) suitable for tandem architectures and superior thermal stability. However, $CsPbI_2Br$ based perovskite solar cells (PSCs) exhibit severe energy loss due to presence of various surface defects like uncoordinated Pb^{2+} ions, halide ion vacancies and pinholes, which causes serious non-radiative recombination and limit the further improvement in power conversion efficiency (PCE). Surface passivation strategy is an effective approach to produce high quality α-$CsPbI_2Br$ film. Herein, we introduce fluorinated ionic liquid, 3-(Trifluoromethyl) benzylamine (CFBA), as surface passivating agent. The chemical analysis shows that the trifluoro (-CF_3) and amine groups of CFBA strongly interacted with perovskite surface via forming Pb-F and H-I bonding, respectively. The high electronegative fluoride atoms of -CF_3 group allow for electrostatic interaction with uncoordinated Pb^{2+} ions, which built a robust shield that protected against surrounding moisture as well. In addition, CFBA modification passivates the dangling bonds, enhanced crystallinity, reduced pinholes, improved the surface coverage and compactness, increased hydrophobicity, and decreased non-radiative recombination, leading to high PCE. With optimum concentration of 3 μL-CFBA, $CsPbI_2Br$ PSC revealed an impressive PCE of 17.07% with FF of 83.21% as compared to pristine device (PCE of 15.24% with FF of 79.81%). Moreover, champion device showed an excellent thermal stability by retaining ~ 86.23% of its initial PCE, whereas pristine device maintained ~ 48.26% of its original PCE after 1440 h aging at 85 ℃ in a dry box without any encapsulation. In addition, optimized PSC showed a decent indoor PCE of 23.24% as compared to pristine device (18.35%) under dim lighting conditions (LED, 3200 K) at 1000 lx. These results suggested that surface passivation strategy with CFBA is a promising approach for developing efficient all-inorganic $CsPbI_2Br$ outdoor/indoor PSCs with better thermal stability.

1. Introduction

In the past decade, organic/inorganic metal halide-based perovskites have gained massive attention due to their ease of fabrication and outstanding optoelectronic properties such as strong optical absorption, high carrier mobility, low exciton binding energy, high defect tolerance, tunable optical bandgap, and long charge carrier diffusion length [1–3]. The certified power conversion efficiency (PCE) of PSCs has rapidly soared from initial 3.8% to the 25.73% [4,5], which is comparable to that of commercial polycrystalline silicon solar cells [6]. Despite remarkable progress in terms of PCE, conventional halide perovskite materials suffer from thermal instability owing to volatility of organic molecules (methylammonium (MA^+) and formamidinium (FA^+)) under high temperature processing, which impedes their future commercial applications [7]. To overcome this issue, substitution of volatile organic components in the halide perovskite materials with inorganic cesium

* Corresponding authors at: Department of Energy Systems Engineering, Chung-Ang University, Seoul 06974, Republic of Korea (D.W. Kang).
E-mail addresses: jscho@cbnu.ac.kr (J.S. Cho), kangdwn@cau.ac.kr (D.-W. Kang).

https://doi.org/10.1016/j.apsusc.2023.157901
Received 12 April 2023; Received in revised form 30 May 2023; Accepted 26 June 2023
Available online 27 June 2023

cations (Cs^+) is an effective strategy [3,8,9].

Recently, all-inorganic $CsPbX_3$ (X: I, Br, Cl, or mixture thereof) perovskite such as $CsPbI_3$, $CsPbBr_3$, $CsPbI_2Br$, $CsPbIBr_2$ have been demonstrated as promising light harvesting materials due to excellent thermal stability as well as tunable optical band edge from 1.73 to 2.3 eV for development of stable PSCs [10–14]. Among these, mixed halide based inorganic $CsPbI_2Br$ perovskite is the most promising candidate with its good intrinsic phase stability, desired tolerance factor (0.84), superior light absorption ability, and reasonable band gap (1.92 eV) for use as a top cell in the fabrication of tandem solar cells (TSCs) [13,15–18]. Nonetheless, PCE of $CsPbI_2Br$ PSCs is still far from Shockley–Queisser (SQ) efficiency limit due to the presence of several defects on the surface and in the bulk of perovskite [19]. The deep level defects are considered as interfacial defects, causing perovskite decomposition and non-radiative recombination, whereas conventional surface defects are halide ion vacancies and uncoordinated lead ions [20,21]. In general, inorganic perovskite films are developed by solvent evaporation of the precursor solution, several defects on the surface or at the grain boundaries (GBs) during the crystallization process are easily formed [20,22,23]. These defects act as non-radiative recombination centers that induce the additional energy loss, and hence limits the device performance [20,23]. Therefore, performance of PSCs can be improved by passivating the defects. The different kind of strategies such as additive engineering, antisolvent engineering, interfacial engineering, metal doping, surface passivation, ion substitution, gradient thermal annealing etc., [3,10,24–29] have been proposed to reduce the number of defects and development of the efficient PSCs. Among them, due to ease of application, surface passivation is an effective way to suppress the defect density of perovskite film [22].

Various molecules have been introduced to passivate the surface and grain boundary defects. For instance, Lewis acids (phosphoric acid [30], carboxylic acid [31], sulphonic groups [32] and so on) and Lewis bases (pyridine [33], imidazole [22], benzoquinone [34], etc.) were used to suppress uncoordinated Pb^{2+} ions. In addition, halide ion vacancies or halide ions deficiency can be compensated by surface passivation of perovskite film with additional halide based organic/inorganic molecules such as phenylethylammonium iodide (PEAI), ethylammonium iodide (EAI), phenylethylammonium bromide (PEABr), 4-fluorophenylethylammonium halides, tetrabutylammonium iodide (TBAI) [13,29,35–37], cadmium iodide (CdI_2) [38], cesium bromide (CsBr) [39], etc. Moreover, pseudohalides such as SCN^-(thiocyanate) [40], $[PF]_6^-$(hexafluorophosphate) [41] and $[BF]_4^-$ (tetrafluoroborate) [42] with similar ionic radii and chemical properties to iodide were also used to passivate the trap densities. Passivation with fluoride ion-based molecules is an efficient approach to mitigate the traps owing to its higher electronegativity, facilitate strong interaction between lead and fluoride ions [22]. For example, Chen et.al treated $CsPbI_2Br$ perovskite film surface with 4-trifluoromethyl phenethylammonium iodide (CFPEAI), and suggested that trap densities significantly passivated, leading to high PCE of 16.07% as compared to control PSC (14.50%) [29].

As for the case of organic/inorganic halide salts, Lewis acids/bases, and polymers, they were employed to passivate the perovskite film surface. However, these surface passivators have insulating properties that hamper the efficient charge extraction phenomena at the perovskite/HTL interface owing to their poor electrical conductivity [43]. In addition, researchers have used cadmium based inorganic halide salt (CdI_2) [38] as a surface passivator, which is toxic owing to presence of highly toxic cadmium content. On the other hand, it has been demonstrated that ionic liquids are promising candidates as surface passivation agents owing to their unique properties including high conductivity, low toxicity, wide liquid temperature range, non-volatile, and good stability [44–47]. In this regard, various ionic liquids such as 1-butyl-2,3-dimethylimidazolium tetrafluoroborate ($BMMIMBF_4$), 1-butyl-3-methylimidazolium iodide (BMIMI), 1-viny-3-propionate ethyl imidazolium chloride ([PEVIM]Cl) etc., effectively passivated the $CsPbI_2Br$ perovskite film surface, resulting in improved device performance and stability [43,44,48]. For example, Xu et.al introduced 1-butyl-2,3-dimethylimidazolium tetrafluoroborate ($BMMIMBF_4$) as a surface passivation agent for $CsPbI_2Br$ perovskite film. They demonstrated that $BMMIM^+$ cation of $BMMIMBF_4$ molecule formed coordinative bond with uncoordinated Pb^{2+} ions, while BF_4^- anion interacted through ionic bond with Pb^{2+}/Cs^+ ions, mitigating non-radiative recombination [43]. Pu et.al employed 1-viny-3-propionate ethyl imidazolium chloride [PEVIM]Cl ionic liquid as a surface passivator. This research group suggested that carbonyl group of [PEVIM]Cl molecule interacted uncoordinated metal ions (Cs^+ and Pb^{2+}) on the perovskite surface. They demonstrated that lone unpaired electron on the oxygen (O) atom donates to the uncoordinated metal, passivating surface traps of $CsPbI_2Br$ perovskite film [48]. Thus, ionic liquids efficiently passivated the surface defects (uncoordinated metal ions), resulting in improved film quality. However, imidazolium based ionic liquids have some limitations as it has been demonstrated that long alky chains and side methyl groups on imidazolium group induce the steric hindrance effects, resulting in impeding the interaction of nitrogen atom on imidazolium group with the CsI or PbI_2 [43]. Therefore, we have chosen 3-(Trifluoromethyl) benzylamine ($CF_3 + C_6H_4CH_2NH_2$ (benzylamine), CFBA) as a new surface passivation agent ionic liquid, which is different from the reported ionic liquids.

Motivated by the above studies, we have exploited a novel fluorinated organic compound as 3-(Trifluoromethyl) benzylamine ($CF_3 + C_6H_4CH_2NH_2$ (benzylamine), CFBA) for surface passivation of $CsPbI_2Br$ perovskite film. A detailed literature survey on surface passivation of $CsPbI_2Br$ perovskite is provided in supporting information (Table S1), to the best of our knowledge for the first time we have introduced CFBA ionic liquid as surface passivating agent to develop high quality $CsPbI_2Br$ perovskite film. We have successfully investigated the effect of CFBA with various concentrations (1, 3 and 5 μL) surface treatment on the crystallinity, microstructural, and optoelectronic properties of the $CsPbI_2Br$ thin films and PSCs. We found that perovskite surface treatment with CFBA significantly passivated defects such as pinholes, voids, and suppressed the uncoordinated Pb^{2+} ions by strong interaction of fluoride ions with Pb^{2+}, and hydrogen bonding with anions. We observed that the trifluoro (-CF_3) and amine (–NH_2) groups of CFBA strongly interacted with the perovskite surface via forming Pb-F bond (electrostatic interaction) and hydrogen bonding (H-I), respectively. The interaction of trifluoro (-CF_3) group with uncoordinated Pb^{2+} ions of perovskite via forming Pb-F bond, passivated the positively charged uncoordinated Pb^{2+} surface defects and amine (–NH_2) group interacts with unsaturated I^-/Br^- ions at perovskite surface through hydrogen bonding (H-I), resulting in suppression of the negatively charged Pb-I anti-site defects (PbI_3^-) and uncoordinated halide (I^-/Br^-) ions. Thus, the additional amine (–NH_2) group further strengthened the interaction of CFBA molecule with perovskite through hydrogen bonding (H-I), effectively passivating the surface defects. The surface treatment of perovskite film with CFBA can also assist the recrystallization that reconstruct the perovskite surface, increasing the crystalline properties of film. As a result, an optimum concentration of CFBA (3 μL) treated PSC reached to an impressive PCE of 17.07% with FF of 83.21% under ambient conditions, which is higher than that of pristine device (PCE of 15.24% with FF of 79.81%). In addition, optimized PSC showed remarkable thermal stability by retaining 86.23% of original PCE, whereas pristine device dropped to 48.26% of initial PCE after storing in a dry box over 1440 h at 85℃. Moreover, champion PSC showed high PCE of 23.24% as compared to pristine PSC (18.35%) under LED lighting conditions (3200 K, 1000 lx). Thus, the proposed strategy provides a feasible method to produce high-quality all inorganic α-$CsPbI_2Br$ perovskite films to achieve a high PCE.

Moreover, as we have additionally provided a detailed literature study especially on the development of $CsPbI_2Br$ based PSCs using different surface passivation agents (Table S1). From Table S1, it is noteworthy that researchers developed $CsPbI_2Br$ based PSCs using a surface passivation strategy under N_2 gas/dry air-filled glovebox, which

is not suitable from the commercialization aspect. The large-scale production of inorganic $CsPbI_2Br$ PSCs is not feasible through N_2 gas filled glovebox process based reported strategies. To address this issue, we have developed an efficient $CsPbI_2Br$ based PSC under ambient atmospheric conditions (average relative humidity range of ~ 32–40%, temperature ~ 21–24 ℃) through surface passivation strategy using CFBA ionic liquid as a surface passivation agent. Even though the ambient air processing for all-inorganic $CsPbI_2Br$ PSCs is a harsh condition compared to the N_2-filled glove box, the device performance is highly encouraging, as indicated in Table S1.

2. Experimental section

2.1. Materials

Isopropanol (IPA, 99.5%), acetone (99%), ethanolamine (99%), 2-methoxyethanol (2-ME, 99%), dimethylformamide (DMF, 99.5%), and dimethyl sulfoxide (DMSO, 99.8%) were acquired from Samchun Chemical. Tin oxide (SnO_2) colloidal solution (15% in H_2O) and cesium iodide (CsI, 99.99%) were purchased from Alfa Aesar. Chlorobenzene (CB, 99% GR grade) and Phenyl-C61-butyric acid methyl ester ($PC_{61}BM$, 99.5%) were purchased from Organic Semiconductor Materials and Wako Chemicals, respectively. Zinc acetate dihydrate (Zn $(CH_3CO)_2{\cdot}2H_2O$, 99.99%), 3-(Trifluoromethyl)benzylamine (CFBA, 98%), 4-*tert*-butylpyridine (tBP), and lead bromide ($PbBr_2$, 99.99%) were bought from Sigma Aldrich. Lead iodide (PbI_2, 99.99%) was purchased from TCI (Tokyo Chemical Industry) Co., Ltd. Tokyo, Japan. Poly (3-hexylthiophene-2,5-diyl) (P3HT) and gold pellets (Au, 99.99%) were purchased from Research and Development Korea corp., respectively. Indium doped tin oxide (ITO)-coated glass substrates with a sheet resistivity of 10 Ω/□ were purchased from AMG, Korea. All the chemicals were used as received without further purification.

2.2. Precursor solution preparation

The SnO_2 precursor solution was prepared by adding 0.3 mL SnO_2 colloidal solution (15% in H_2O) into 2.7 mL deionized water (DI) and then stirred for 12 h at room temperature. The ZnO precursor solution was obtained by mixing 0.2195 g into 2 mL 2-ME and 61.7 μL ethanolamine, stirred at 60℃ for 2 h. For 1.2 M $CsPbI_2Br$ perovskite precursor solution, 0.3118 g of CsI, 0.2776 g of PbI_2 and 0.2202 g of $PbBr_2$ were mixed into 0.7 mL DMSO and 0.3 mL DMF and then stirred inside glovebox overnight at room temperature (RT) to form a transparent solution. Before use, SnO_2, ZnO and perovskite precursor solutions were filtered through 0.2-μm hydrophilic syringe filter (Advantec). For CFBA precursor solutions, different amounts of CFBA (1, 3 and 5 μL) were mixed individually into 1 mL IPA, followed by stirring at RT overnight. The P3HT precursor solution was formed by dissolving 10 mg P3HT into the 1 mL CB and 20 μL tBP. A 20 mg amount of $PC_{61}BM$ was added into 0.75 mL CB and 0.25 mL DCM, stirred overnight at RT for obtaining $PC_{61}BM$ solution. The prepared CFBA solution was filtered using 0.2-μm hydrophilic syringe filter (Advantec). The P3HT and $PC_{61}BM$ solutions were filtered using 0.2-μm hydrophobic syringe filter (Advantec).

2.3. Fabrication of perovskite solar cells

The procedure for fabrication of PSCs is demonstrated in Fig. S1. In detail, ITO (indium doped tin oxide) coated glass substrates were cleaned sequentially with acetone and isopropanol in ultra-sonication bath for 20 min in each solvent, and then kept for drying in oven at 95 ℃ for 30 min. The dried substrates were treated with ultraviolet-ozone (UV-O_3) for 20 min to increase the wettability and remove organic impurities if present at the surface. The SnO_2 precursor solution was spin-coated onto the ITO substrates at 1000 rpm for 0.5 s and 3000 rpm for 30 s successively, and then annealed at 150 ℃ for 30 min. Then, ZnO precursor solution was deposited onto the SnO_2/ITO substrates with continuous spinning speed of 1000 rpm and 5000 rpm for 0.5 s and 30 s, respectively, and then heated at 170 ℃ for 30 min. Afterward, $CsPbI_2Br$ perovskite precursor was spin-coated at 3000 rpm for 40 s on top of ZnO/SnO_2/ITO substrates. During spin coating of perovskite solution from 8 to 22 s, dynamic hot air (230 ℃) was blown using dynamic hot air gun (BOSCH, GHG 630 DCE Hot Air Gun − 0601 94C 740) onto the substrates to stimulate the nucleation of perovskite crystal. After completing the spin coating process, substrates were immediately annealed at 240 ℃ for 10 min. The procedure of dynamic hot air method (in detail) was mentioned in the supplementary information (Fig. S2 and Fig.S3(a)). To obtain CFBA treated perovskite film, CFBA solution was spin coated on top of perovskite/ZnO/SnO_2/ITO substrates at 3000 rpm for 30 s, and then annealed at 100 ℃ for 5 min (Fig. S3(b)). Subsequently, P3HT solution was coated on the CFBA treated substrates at 3000 rpm for 30 s and then sintered at 100℃ for 5 min. For SCLC measurement, the electron only devices were prepared by depositing $PC_{61}BM$ solution on CFBA treated substrates at 1500 rpm for 30 s and then heated at 70 ℃ for 10 min. Finally, 80 nm thick gold (Au) metal electrode was deposited by thermal evaporator at ~ 3.0×10^{-6} Torr. The active area of cell is defined as 0.04 cm^2 using a shadow mask. Note that α-$CsPbI_2Br$ perovskite film and different concentration (1, 3 and 5 μL) CFBA treated perovskite films are referred to as pristine, pristine + 1 μL CFBA, pristine + 3 μL CFBA, and pristine + 5 μL CFBA, respectively. The detailed information of characterization techniques was demonstrated in the supplementary information.

3. Results and discussion

We have developed high quality α-$CsPbI_2Br$ perovskite thin film under ambient conditions (average relative humidity range of ~ 32–40%, temperature ~ 21 – 24 ℃) using surface passivation strategy. In this approach, pristine α-$CsPbI_2Br$ perovskite film surface was treated with various concentrations (1, 3, and 5 μL) of CFBA ionic liquid in IPA solutions. To examine the interaction of CFBA with pristine perovskite film, we performed FTIR and liquid-state ^{13}C NMR measurements, obtained patterns were presented in Fig. 1(a) and Fig. 1(b), respectively. The FTIR spectrum of CFBA molecule showed a dominant peak as appeared at 1327 cm^{-1}, confirmed the existence of -CF_3 bond [49]. In addition, the CFBA FTIR pattern showed the peaks at ~ 1507 cm^{-1} and ~ 1558 cm^{-1}, representing the presence of C = C stretching vibration (from benzene ring) [50,51] and N–H bending (from amine group) [52], respectively.

The FTIR pattern of inorganic α-$CsPbI_2Br$ pristine film is well consistent with reported works [53–55]. Compared to pristine thin film, 3 μL CFBA treated perovskite film showed additional characteristic peaks as centered at ~ 1330 cm^{-1}, ~ 1507 cm^{-1} and ~ 1559 cm^{-1}, which can be assigned to -CF_3 bond (Fig. 1(a) and Fig. S4(a)), –NH bending (Fig. 1(a) and Fig. S4(b)), and C = C stretching vibration (Fig. 1 (a) and Fig. S4(c)), respectively, confirming the existence of CFBA molecule in the resulting perovskite film (CFBA treated $CsPbI_2Br$ perovskite). It is noteworthy that a slight shift was observed in peaks of -CF_3 group (Fig. S4(a)) and N–H bending (Fig. S4(b)) towards the lower wavenumber, confirming that highly electronegative fluoride ions as associated with -CF_3 group interacted with uncoordinated Pb^{2+} ions of perovskite through coulombic/electrostatic interaction (by forming Pb-F bond) and hydrogen of amine group (–NH_2) interacted with halide (iodide/bromide) ions of perovskite through hydrogen bonding (-N–H……..I/Br), respectively. Thus, FTIR analysis clearly suggested an interaction of CFBA molecule with pristine ($CsPbI_2Br$) perovskite film. The liquid-state ^{13}C NMR measurement for neat CFBA and CFBA-PbI_2 was performed in deuterated DMSO-d_6 (Fig. 1(b)). The simulated ^{13}C NMR pattern of neat CFBA organic molecule was depicted in Fig. S5, in which resonance signals related to each carbon position of CFBA were demonstrated. The experimental ^{13}C NMR spectrum of neat CFBA molecule displayed a resonance signal at ~ 125.35 ppm corresponding to the carbon position as associated with fluoride ions (Fig. 1(b)). After

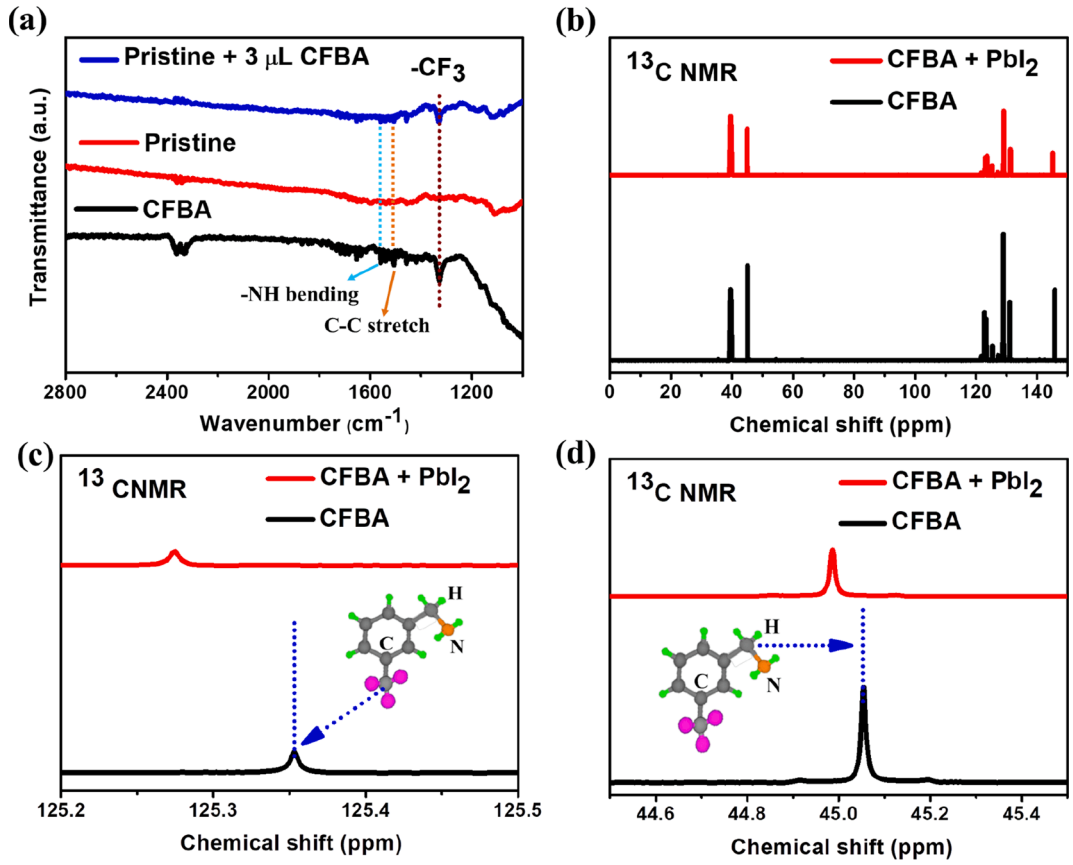

Fig. 1. (a) FTIR of CFBA molecule, pristine and pristine + 3 μL CFBA perovskite films; (b) ^{13}C NMR of CFBA and CFBA + PbI_2; (c) Enlarged ^{13}C NMR spectrum of carbon linked with -CF_3 group from 125.2 to 125.5 chemical shift (ppm), (d) Enlarged ^{13}C NMR spectra of carbon associated with amine group (–NH_2) from 44.5 to 45.5 chemical shift (ppm).

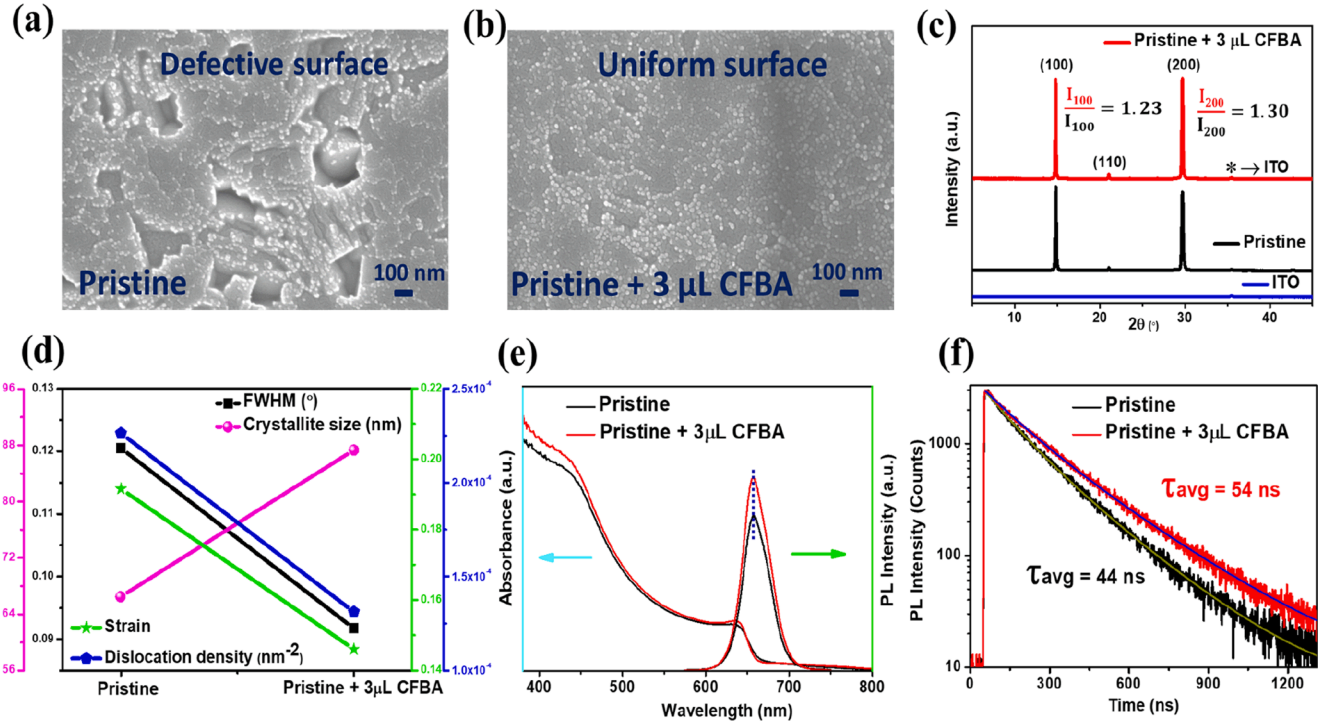

Fig. 2. FESEM top view of (a) pristine and, (b) pristine + 3 μL CFBA perovskite films; (c) XRD patterns of ITO substrates, pristine and pristine + 3 μL CFBA perovskite films; (d) Calculated FWHM, average crystallite size, strain, and dislocation density, (e) UV–visible patterns and steady-state photoluminescence spectra, and (f) Time-resolved photoluminescence spectrums for pristine and pristine + 3 μL CFBA perovskite films.

addition of PbI_2, carbon position of -CF_3 group of CFBA molecule was shifted towards lower value of ppm as shown in enlarged spectrum (Fig. 1(c)), it signifies stronger interaction between $CsPbI_2Br$ and CFBA molecule through Pb-F bonding. The highly electronegative three fluoride ions as linked with -CF_3 group permit coulombic interaction with uncoordinated Pb^{2+} ions, resulting suppressed Pb^{2+} dangling bond defects. Moreover, as shown in Fig. 1 (d) (^{13}C NMR enlarged spectrum), carbon position as connected with –NH_2 group shifted towards lower ppm value, also indicating interaction of CFBA molecule with perovskite surface via H-I bonding. The interaction of –NH_2 amine group with unsaturated halide ions (I^-/Br^-) through hydrogen bonding passivating the negatively charged Pb-I anti-site defects (PbI_3^-) and uncoordinated halide (I-/Br-) ions.

To investigate the top surface morphology of without and with CFBA treated perovskite films, FE-SEM measurement was conducted. The captured top-view scanning SEM images of pristine and different concentration of CFBA (1, 3 and 5 μL) treated perovskite films were depicted in Fig. 2(a, b) and Fig. S6 (a, b). The pristine perovskite film (Fig. 2(a)) demonstrated poor morphology with pinholes, voids, rough and non-uniform surface, which might serve as non-radiation recombination centers. When pristine perovskite film surface was treated with 1 μL CFBA solution, film morphology improved, however, still minor rough surface observed in the film (Fig. S6(a)). Interestingly, as concentration of CFBA treatment increased from 1 to 3 μL, pinholes significantly suppressed, uniform and compact morphology were obtained (Fig. 2 (b)). This modulation in morphology indicates that CFBA treatment effectively reconstructed the perovskite surface owing to strong interaction between Pb-X framework and CFBA molecule by forming bond between uncoordinated Pb^{2+} ions (electron-deficient) and F^- ions (electron rich) (Pb-F), and hydrogen bonding (H-I), resulting improved film quality [29,43]. After CFBA deposition, the post annealing process (100 ℃@5min) would facilitate the secondary crystallization at the top surface, and interaction of CFBA molecule through Pb-F and H-I bonding with perovskite mitigated the surface perovskite defects, results in reconstructing the perovskite surface. It has been explored that deposited organic molecules on the perovskite surface promotes secondary crystallization of perovskite during thermal annealing process, leading to compact perovskite morphology [56,57]. Moreover, it has also been demonstrated that the surface passivation strategy with organic molecules reconstruct the perovskite surface, resulting in formation of the compact perovskite film [58]. However, when further increased concentration of CFBA to 5 μL, surface morphology of film was degraded (Fig. S6(b)). Obviously, a slight change in topography of 5 μL CFBA assisted perovskite film as compared to the optimized (3 μL) sample was observed, which might be due to excess CFBA concentration. An excess concentration of CFBA contains large number of highly electronegative fluoride ions that would repel the existed halide (I^-/Br^-) ions (in lattice $[PbX_6]^{4-}$ octahedron) at perovskite surface due to same polarity of charges as shown in schematic diagram (Fig. S7). It results in distortion of the $[PbX_6]^{4-}$ octahedron of crystal structure. Thus, we speculate that large number of high-electronegative fluoride ions with excess concentration of CFBA may induce lattice strain in the perovskite crystal by disturbing the existed Pb-X bonds in the $[PbX_6]^{4-}$ octahedron of crystal structure, which might degrade also the surface morphology of film. Thus, an optimum concentration of CFBA (3 μL) treatment showed favorable impact on the surface morphology.

To examine the influence of CFBA molecule on the crystallinity of pristine perovskite, XRD patterns were recorded as shown in Fig. 2(c) and Fig. S8(a-b) The pristine film exhibited distinctive peaks at 14.80° (100), 21.04° (110), and 29.69° (200), confirmed the formation of α-phase $CsPbI_2Br$ [17,39,59]. After 3 μL CFBA surface treatment, characteristic peaks were obtained at almost the same value of 2θ, indicating CFBA molecule does not enter into the crystal lattice. Noticeably, diffraction peaks ((100) and (200)) intensities significantly enhanced in case of 3 μL CFBA treated perovskite film. The individual peak intensity ratio like I_{100}(3 μL-CFBA)/I_{100}(pristine) and I_{200}(3 μL-CFBA)/I_{200}(pristine) were found to be 1.23 and 1.30, respectively (Fig. 2(c)), reveals crystallinity of 3 μL-CFBA assisted perovskite film remarkably increased as compared to pristine. Notably, CFBA treated perovskite film showed higher crystallinity than pristine one. It is mainly attributed to secondary crystallization at the top of perovskite surface. The annealing process (100℃ for 5 min) after CFBA treatment would facilitate the secondary crystallization at the top surface, resulting in improved the film crystallinity. However, when concentration of CFBA increased to 5 μL, diffraction peaks (100) and (200)) intensity reduced as compared to pristine + 3 μL CFBA perovskite film, which indicates that film quality was degraded with excess concentration of CFBA, and consistent with FESEM results. Moreover, pristine + 5 μL CFBA perovskite film exhibited a noticeable peak shift towards lower angle as displayed in Fig. S8(b), indicating lattice expansion [14,60]. This phenomenon could be ascribed to the excess fluoride ions (highly electronegative) that can induce tensile strain by repelling existed halide ions (I^-/Br^-) (in lattice $[PbX_6]^{4-}$ octahedron) at the perovskite surface due to same polarity of charges, disturbing the Pb-X bond in $[PbX_6]^{4-}$ octahedron of crystal structure (as shown in Fig. S7). Thus, excess concentration of CFBA might cause a distortion in crystal lattice structure of perovskite, leading to defective surface morphology. Moreover, the average crystallite size, full width at half maxima (FWHM), strain and dislocation density were determined (Fig. 2(d)) for detailed analysis. The average crystallite size was calculated using Debye-Scherrer formula (eq.1) as following [61,62]:

$$D = \frac{k\lambda}{\beta\cos[\theta]} \tag{1}$$

where, D is average crystallite size (nm), k is shape factor (0.9), ʎ is wavelength of X-ray (Cu-Kα radiation, 1.54 Å), β is FWHM (), and θ is diffraction angle (). According to the Williamson-Hall equation (eq. (2), micro-strain and average crystallite size are correlated as [61]:

$$\beta\cos\theta = \frac{k\lambda}{D} + 4\varepsilon\sin\theta \tag{2}$$

Therefore, micro-strain can be expressed as [63]:

$$\varepsilon = \frac{\beta}{4\tan\theta} \tag{3}$$

where, ε, β and θ are the micro-strain, FWHM () and diffraction angle (), respectively.

Moreover, dislocation density can be obtained by following equation [64]:

$$\delta = \frac{n}{D^2} \tag{4}$$

where, δ is dislocation density, and n is a factor, the value of n is almost one for minimal dislocation density.

The eq.1, eq.3 and eq.4 were used to estimate the average crystallite size, micro-strain, and dislocation density, respectively and obtained crystalline parameters were depicted in Table S2 and as well as in shown in Fig. 2(d). After 3 μL CFBA treatment, value of FWHM decreased and average crystallite size increased, indicating that crystalline property of film ameliorated [65]. Generally, micro-strain within the nanocrystalline materials as well as in thin films induce owing to presence of various defects like point defects (site disorder, vacancies), crystal imperfections, and dislocations [61]. Noteworthy, micro-strain and dislocation density decreased after surface modification with 3 μL CFBA, suggesting that defects considerably reduced. These results showed a better interaction of 3 μL CFBA ionic molecule with pristine perovskite, resulting in improved film quality.

To figure out the influence of CFBA treatment on optoelectronic properties of $CsPbI_2Br$ thin film, UV–visible measurement performed and obtained patterns were shown in Fig. 2(e). Notably, CFBA treated perovskite film exhibits slightly higher absorption than pristine film,

revealing film quality improved [66], and defects like band-edge trap states, are considerably reduced [8]. Moreover, enhancement in crystallinity and surface coverage of film is beneficial to increase the light absorbance [17,67]. From Fig. S9 (Tauc plots), both perovskite films showed nearly identical optical band edge of ~ 1.88 eV, which is well consistent with reported works [8,19,68].

To explore the charge carrier dynamics of pristine and CFBA treated perovskite films, steady-state photoluminescence (PL) and time-resolved photoluminescence (TR-PL) spectrums were recorded as depicted in Fig. 2(e) and Fig. 2(f), respectively. As compared to pristine film, CFBA treated perovskite film shows high PL intensity (Fig. 2(e)), manifesting that spontaneous non-radiative recombination remarkably was suppressed owing to passivation of surface defects [17,66,69,70]. The TRPL curves were fitted using a bi-exponential decay function of time as following [8,71]:

$$F(t) = A_1 exp\left(-\frac{t}{\tau_1}\right) + A_2 exp(-\frac{t}{\tau_2}) \quad (5)$$

where, short lifetime (τ_1) represents the surface (non-radiative) recombination that originates from the surface traps near the grain boundaries, long lifetime (τ_2) indicates the bulk (radiative) recombination in the bulk film; A_1 and, A_2 are the associated amplitudes. The fitted decay parameters corresponding to pristine and CFBA treated perovskite films were demonstrated in Table S3. Interestingly, after CFBA treatment, the values of τ_1 and τ_2 lifetimes are prolonged from 24.17 to 29.53 ns and from 47.10 to 59.86 ns, respectively, confirmed that both surface and bulk recombination suppressed owing to improvement in crystallinity and film morphology. Moreover, the average carrier lifetime (τ_{avg}) was obtained using following equation [17]:

$$\tau_{avg} = \frac{A_1\tau_1^2 + A_2\tau_2^2}{A_1\tau_1 + A_2\tau_1} \quad (6)$$

From eq. (6), the value of τ_{avg} corresponding to pristine and CFBA treated perovskite films were calculated to be 44 ns and 54 ns (Table S3), respectively. Notably, CFBA assisted perovskite film showed longer carrier lifetime as compared to pristine, which also confirms that trap-assisted recombination significantly diminished with CFBA treatment.

To identify the impact of CFBA treatment on photovoltaic performance, we fabricated PSCs with n-i-p (ITO/SnO_2/ZnO/perovskite/P3HT/Au) configuration as depicted in schematic diagram (Fig. 3(a)). The measured current density–voltage (*J-V*) characteristics of pristine and different concentration of CFBA based PSCs were demonstrated in Fig. 3(b) and Fig. S10. The obtained photovoltaic (*PV*) parameters corresponding to without and with various concentration of CFBA assisted PSCs were listed in Table 1 and Table S4. The pristine device exhibited a PCE of 15.24% with current density (J_{sc}) of 15.83 mA/cm^2, open circuit voltage (V_{oc}) of 1206 mV and fill factor (FF) of 79.81%. After 1 μL CFBA treatment, PSC showed an improvement in PV parameters like PCE of 16.36% with J_{sc} of 15.94 mA/cm^2, V_{oc} of 1245 mV and FF of 82.40%. When concentration of CFBA increase to 3 μL, device PV parameters

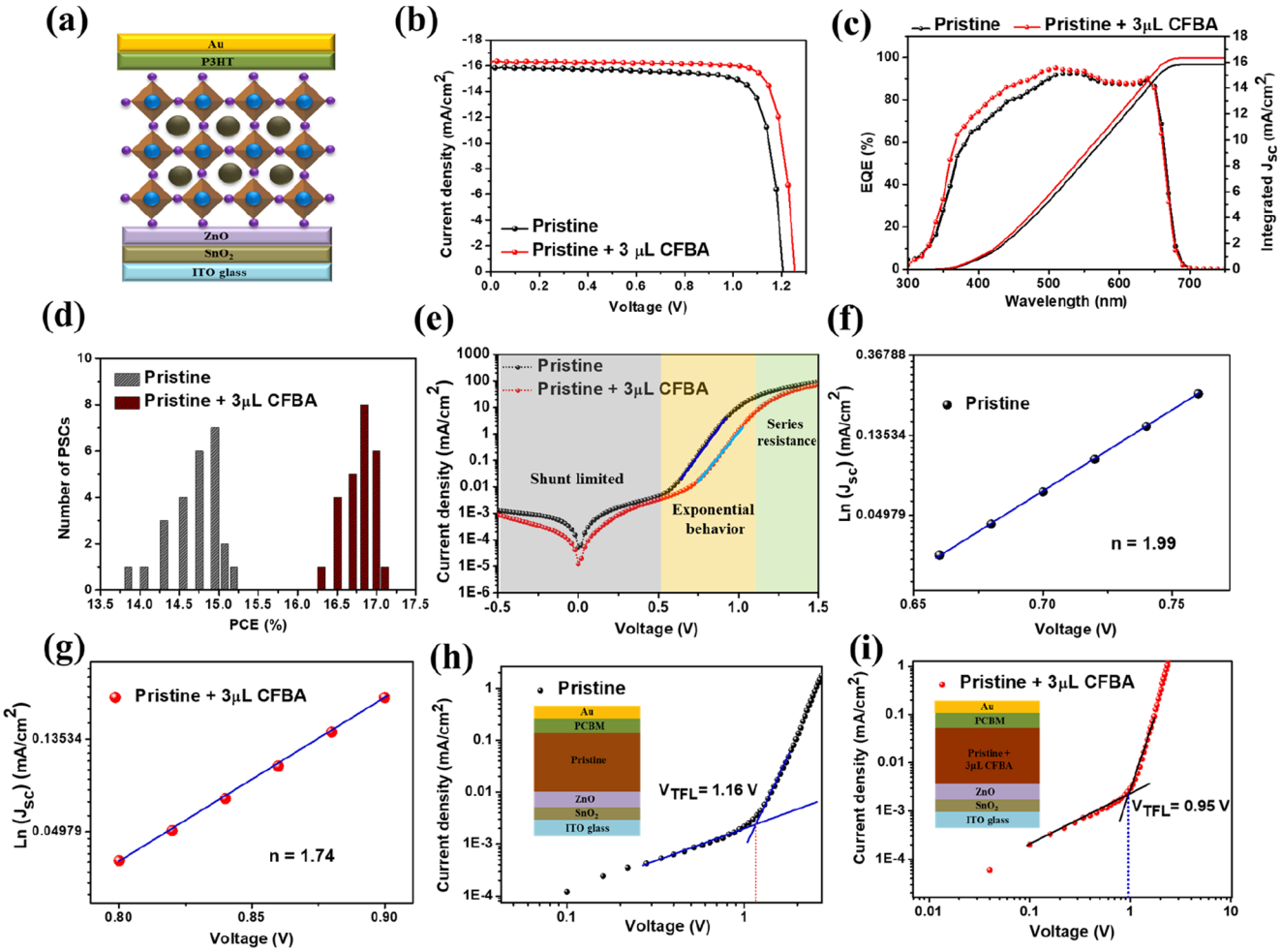

Fig. 3. (a) Schematic representation of fabricated PSC with n-i-p structure; (b) Current density–voltage curves, (c) EQE and integrated current density–voltage spectrums, (d) PCEs histogram for pristine and 3 μL CFBA assisted PSCs; (e) Dark current density–voltage patterns of pristine and 3 μL CFBA assisted based PSCs; Calculated ideal factor for (f) pristine and (g) 3 μL treated PSCs; Space charge-limited current spectra for (h) Pristine PSC, and (i) 3 μL CFBA treated PSC.

Table 1
PV parameters of pristine, and 3 μL CFBA assisted PSCs.

Devices	J_{SC} (mA/cm^2)	V_{OC} (mV)	FF (%)	PCE (%)
Pristine	15.83	1206	79.81	15.24
Pristine + 3 μL CFBA	16.35	1255	83.21	17.07

further increased as PCE of 17.07% with J_{sc} of 16.35 mA/cm^2, V_{oc} of 1255 mV, and FF of 83.21%. Such considerable increment in PV parameters attributed to reduced trap-assisted recombination, enhanced crystallinity, improved surface morphology of perovskite film after surface treatment with 3 μL CFBA. However, when further CFBA concentration increased to 5 μL, a reverse trend was observed, and device PV parameters decreased as PCE of 16.36% with J_{sc} of 15.94 mA/cm^2, V_{oc} of 1245 mV and FF of 82.40%, might be due to excess concentration that degraded the film morphology (Fig. S6(b)). Thus, 3 μL CFBA assisted PSC exhibited an impressive PCE of 17.07%, considered to be a champion device, and as per the systematic literature study (Table S5), obtained champion PCE (17.07%) is one of high performance in case of inorganic pristine PSCs. In addition, we recorded external quantum efficiency (EQE) patterns of pristine and 3 μL CFBA treated PSCs as depicted in Fig. 3(c). In comparison to pristine PSC, 3 μL CFBA assisted device exhibited higher EQE value, might be due to suppressed charge carrier recombination, higher light absorbance, and improved film quality. From EQE spectrums, the integrated J_{sc} was calculated to be 15.81 mA/cm^2 (pristine) and 16.34 mA/cm^2 (3 μL CFBA), which is well consistent with J-V characteristics values. To confirm the reproducibility, we constructed 25 individual devices of both cases (pristine and 3 μL CFBA) and obtained PCEs displayed in Fig. 3(d) (histogram). The 3 μL CFBA assisted PSCs showed narrow PCE distribution as compared to pristine devices, elucidating the good reproducibility.

To evaluate the leakage current in the fabricated PSCs, dark current density–voltage measurement was performed for with and without CFBA treated devices. As shown in Fig. 3(e), 3 μL CFBA assisted PSC exhibited lower value of dark current as compared to pristine device, implies that leakage current reduced after CFBA treatment. A decrement in leakage current indicates defective pinholes and grain boundary traps significantly diminished [44,72,73]. The Shockley diode equation as mentioned below [74,75]:

$$J_{dark} = J_0[\exp\left(\frac{qV}{nK_BT}\right) - 1] \quad (7)$$

where, J_{dark} is the dark current density, J_0 is the reverse saturation current, q is elementary charge, V is applied voltage, n is ideal factor, K_B is Boltzmann constant, and T is an absolute temperature. Ideally, the value of n should approach to unity in the absence of charge recombination [75]. The ideal factor n can be determined from slope of exponential behavior regime as displayed in Fig. 3(e). The value of n calculated to be 1.99 and 1.74 corresponding to pristine and 3 μL CFBA assisted PSCs (Fig. 3(f, g)), respectively. The decreased ideal factor value with 3 μL CFBA treatment indicates a better diode junction quality, due to reduced non-radiative recombination [44,76]. According to the following equation [17,77], V_{oc} is strongly dependent on logarithmic ratio of J_{sc} and J_{dark}.

$$V_{oc} = \frac{K_BT}{q} ln(\frac{J_{sc}}{J_{dark}}) \quad (8)$$

where V_{oc}, K_B, T, q, J_{sc} and J_{dark} are the open circuit voltage, Boltzmann constant, absolute Kelvin temperature, electronic charge, short circuit current density, and dark current density, respectively. As compared to pristine device, CFBA assisted PSC showed improvement in J_{sc} and reduction in J_{dark} that leading to high V_{oc} of 1255 mV, suggesting trap-assisted charge carrier recombination significantly decreased.

To quantify the trap-assisted defect density, space charge limited current (SCLC) measurement was conducted by fabricating electron-only-devices (ITO/SnO_2/ZnO/perovskite/PCBM/Au) and recorded dark current–voltage curves displayed in Fig. 3(h, i) for pristine and 3 μL CFBA based devices, respectively. From obtained patterns, trap filled limited voltage (V_{TFL}) can be extracted at the kink point, which signifies the transition of curve from ohmic to trap-filled limited region (as showing in Fig. 3(h, i)) [3]. The value of V_{TFL} corresponds to pristine and 3 μL CFBA assisted devices were found to be 1.16 V and 0.95 V, respectively. The trap density can be estimated by using following formula [8,78]:

$$n_t = \frac{2\varepsilon\varepsilon_o V_{TFL}}{eL^2} \quad (9)$$

where n_t, ε, ε_o, V_{TFL}, e and L are the trap state density, relative dielectric constant (for $CsPbI_2Br$ is 8.5) [8], vacuum permittivity, trap filled limited voltage, elementary charge, and thickness of perovskite film, respectively. According to eq. (9), trap-state density directly proportional to the trap filled limited voltage. Thus, electron trap-state densities were calculated to be 7.96×10^{-15} cm^{-3} and 6.52×10^{-15} cm^{-3} for pristine and 3 μL CFBA treated-devices, respectively. The decreased trap-state density suggesting that perovskite surface effectively passivated after 3 μL CFBA modification, resulting in defects remarkably suppressed, which is conducive to reduce the energy losses. According to the formula as following [79]:

$$E_{loss} = E_g - eV_{oc} \quad (10)$$

Where E_{loss}, E_g, e and V_{oc} indicate energy loss, optical band edge, electronic charge, and open circuit voltage. From eq. (10), calculated energy losses corresponding to pristine and 3 μL CFBA based PSCs were demonstrated in Fig. S11. Noteworthy, energy loss decreased after 3 μL CFBA treatment due to improved film quality.

To evaluate the charge carrier recombination dynamics, electrochemical impedance spectroscopy (EIS) measurement was performed under dark conditions. The EIS curves were recorded at a bias voltage of 1.0 V with frequency range of 100 Hz to 2 MHz corresponding to pristine and 3 μL CFBA based PSCs. As shown in Fig. 4(a), the EIS patterns were fitted using Z-view software according to the equivalent circuit diagram (inset of Fig. 4(a)), which consists of series resistance (R_s), recombination resistance (R_{rec}), and chemical capacitance (C) [80,81]. From Nyquist plots (Fig. 4(a)), the values of R_s and R_{rec} can be obtained corresponding to intercept on the Z'(Ω) axis at a high frequency and diameter of semicircle, respectively [69,82]. In general, R_s induces in the PSCs from different factors like, ITO electrode interface, metal electrode interface and metal wires [83,84], while R_{rec} originates from recombination centers at ETL/perovskite interface [85,86]. The extracted Nyquist parameters were demonstrated in Table S6. The value of R_s is almost similar for with and without CFBA treated PSCs owing to same device architecture [81]. However, it is worth to note that 3 μL CFBA assisted device exhibited higher R_{rec} value of 5042 Ω as compared to pristine PSC (3117 Ω), indicating surface non-radiative recombination sites effectively suppressed after CFBA modification [8,87], which is consistent with SCLC findings.

Further to probe the charge carrier transportation and recombination dynamics, the transient photocurrent (TPC) and transient photovoltage (TPV) decays were measured as depicted in Fig. 4(b) and Fig. 4(c), respectively. From Fig. 4(b), charge carrier transport lifetime (τ_{ct}) was estimated to be 0.75 μs and 1.04 μs corresponding to with and without CFBA treated devices, respectively. As a result, 3 μL CFBA based PSC showed fast decay as compared to pristine device (Fig. 4(b)), confirms the efficient extraction and transportation of photo-generated charge carriers [54]. The enhancement in charge extraction and transport properties is mainly owing to construction of high-quality perovskite film with 3 μL CFBA modification. From TPV decays (Fig. 4(c)), charge carrier recombination lifetime (τ_{rec}) was calculated to be 1.54 μs and 4.84 μs for pristine and 3 μL CFBA assisted PSCs, respectively. Notably,

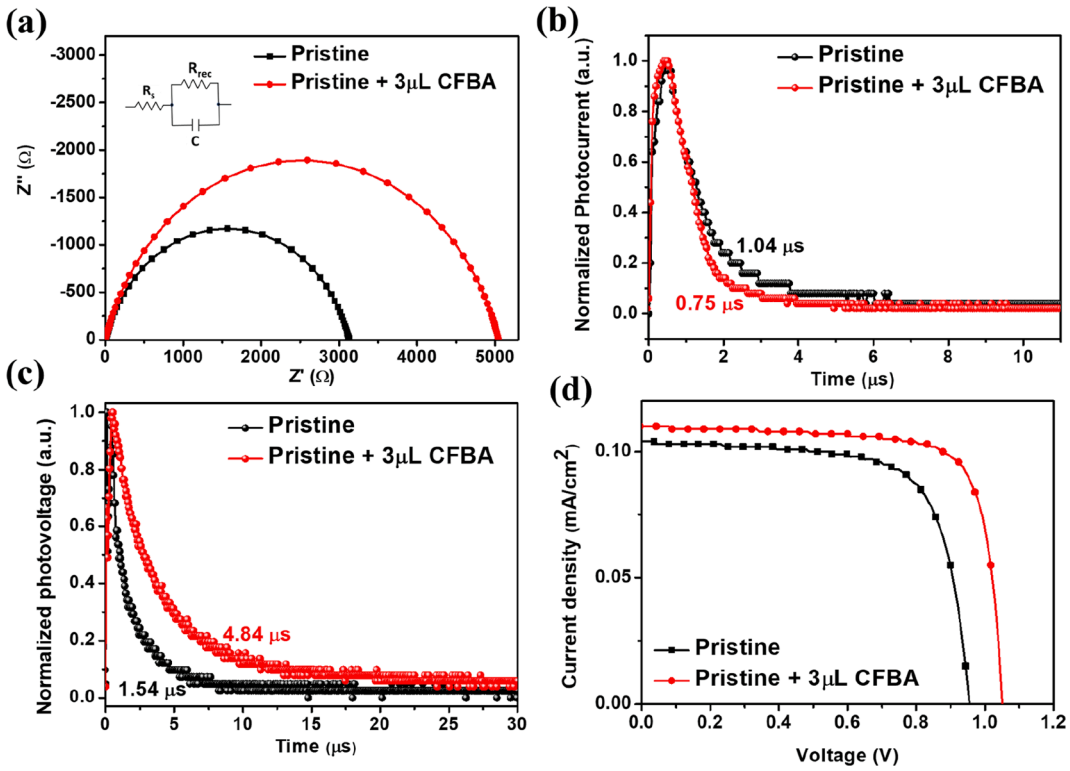

Fig. 4. For pristine and 3 μL CFBA assisted PSCs (a) Electrochemical impedance spectroscopy patterns, (b) Transient photocurrent decay curve, (c) Transient photovoltage decay curve, and (d) Indoor current density–voltage curves.

after 3 μL CFBA treatment, value of τ_{rec} elongated from 1.54 to 4.84 μs, manifesting that trap-assisted defect states substantially suppressed [17], which is in good agreement with EIS and TRPL results. Therefore, 3 μL CFBA treated device exhibited better extraction and transportation phenomena, inhibited nonradiative-recombination, and decreased energy losses, resulting in higher V_{oc} and FF.

In the current scenario, energy generation under low light conditions is a key component of social development. The indoor PSCs can be considered as efficient power sources under dim light conditions to meet the energy requirements to the fast-growing fields (internet-of-things (IoTs)) based applications [88,89]. Consequently, we investigated the indoor photovoltaic (*PV*) performance of pristine and optimized PSCs under the irradiation of light-emitting diode conditions (LED, 3200 K) at 1000 lx, which is a typical day light. The measured indoor current density–voltage (*J-V*) curves of pristine and 3 μL CFBA based PSCs displayed in Fig. 4(d), and corresponding indoor PV parameters were shown in Table 2. The input power density of 382 μW/cm^2 for white LED (3200 K, 1000 lx) was used to determine the indoor PCE. The pristine device showed a power density of 70.10 μW/cm^2 with PCE of 18.35%, J_{sc} of 104 μA/cm^2, V_{oc} of 955 mV and FF of 70.59%. After 3 μL CFBA modification, PSC exhibited a power density of 88.77 μW/cm^2 with PCE of 23.24%, J_{sc} of 110 μA/cm^2, V_{oc} of 1051 mV and FF of 76.79%. The notable increment in indoor PV parameters also suggesting that trap-assisted non-radiative recombination effectively reduced due to enhanced crystallinity and improved film coverage with 3 μL CFBA treatment. In comparison to 1-sun PCE, PSCs show high PCE under indoor (LED) lighting conditions owing to the narrower spectral band that reduces thermalization losses and transparency losses as associated with broadband solar spectrum (1-Sun) [90,91]. From these reasons, generally, the indoor PCE value is higher than the one measured under 1-sun lighting condition.

Table 2
Indoor PV parameters for pristine, and 3 μL CFBA treated PSCs.

Devices	J_{SC} (μA/cm^2)	V_{OC} (mV)	FF (%)	P_{indoor} (μW/cm^2)	PCE (%)
Pristine	104	955	70.59	70.10	18.35
Pristine + 3 μL CFBA	110	1051	76.79	88.77	23.24

From commercialization aspect, optimized PSC can be enabled to power different electronic portable devices like calculator, wrist watches, quartz oscillator, radio frequency identification (RFID), LoRa Backscatters, low powered based sensors, etc. as shown in schematic diagram (Fig. S12) [92–94].

To monitor the long-term thermal stability of constructed PSCs, an aging test was performed over 1440 h at 85 ℃ in dry box (relative humidity range of 10–20%, temperature of 24 – 27 ℃) without any encapsulation of PSCs. As displayed in Fig. 5(a), 3 μL CFBA treated device retained ~ 86.23% of its original PCE, whereas pristine PSC maintained ~ 48.26% of its initial PCE after tracking of 1440 h at 85 ℃ in dry box. It is noteworthy that the optimized PSC exhibited superior long-term thermal stability as compared to pristine device, which is mainly attributed to decreased pinholes, uniformity, dense morphology, good crystallinity, and effective surface defect passivation after 3 μL CFBA modification that stabilize the PCE under thermal stress. Furthermore, to explain the cause of improvement in thermal stability, we investigated the hydrophobicity of perovskite film with and without 3 μL CFBA treatment by measuring the contact angles with deionized water as shown in Fig. 5(b). The contact angle (CA) was estimated to be 46.10° and 62.90° related to the pristine and 3 μL CFBA assisted perovskite films, respectively. As compared to pristine film, 3 μL CFBA treated perovskite film exhibited higher contact angle, indicating that increased humidity resistance of optimized film [17], due to presence of -CF_3 hydrophobic functional group and long alkyl chain [95]. Thus, after 3 μL CFBA modification, the improved hydrophobic nature of perovskite film protected from moisture content, resulting in enhanced thermal stability of the optimized PSCs [29].

Based on the above findings, the key role of CFBA ionic liquid is shown in the schematic diagram (Fig. 5(c)). The CFBA ionic liquid

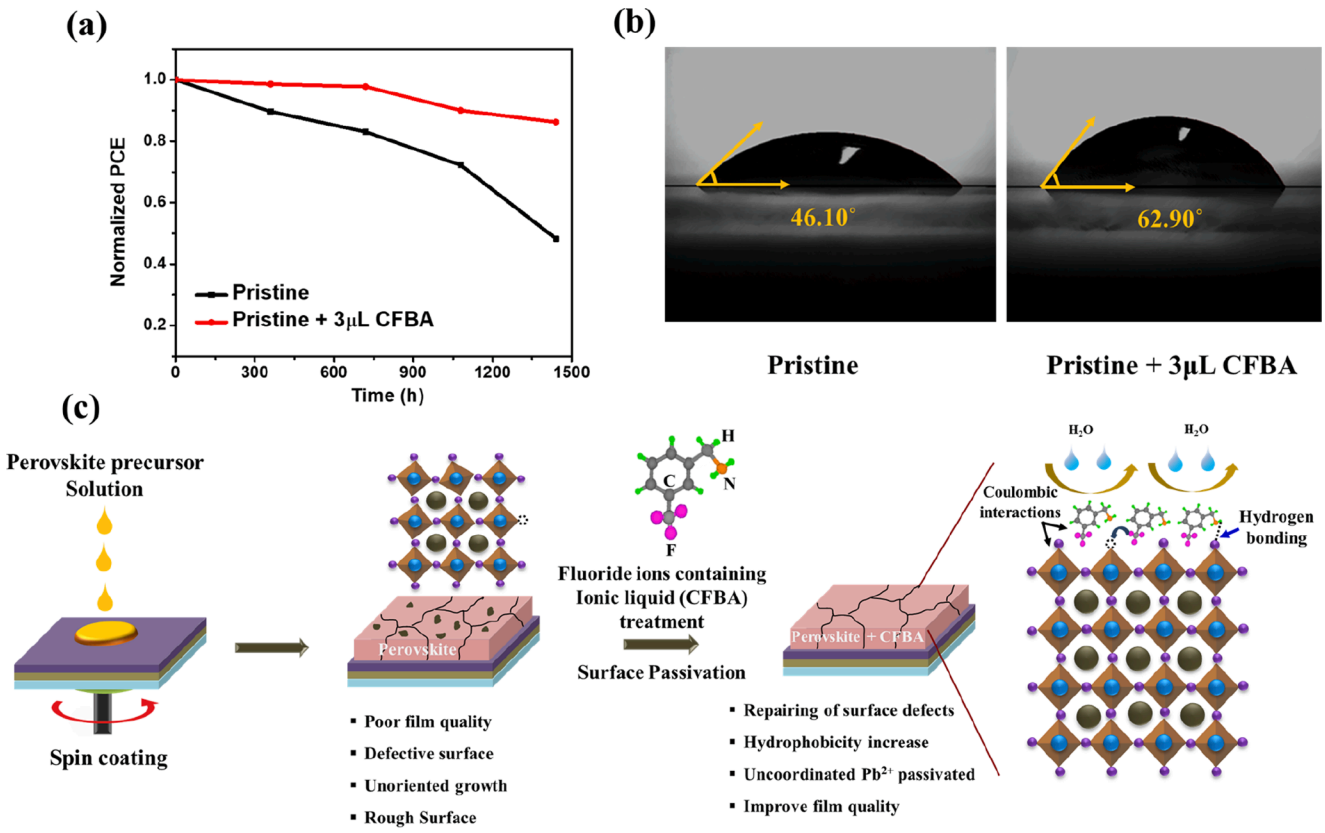

Fig. 5. (a) Thermal stability analysis of pristine and 3 μL CFBA assisted PSCs after aging in dry box at 85 °C (b) Contact angle measurements corresponding to pristine and 3 μL CFBA treated perovskite films, and (c) Schematic illustration of pristine perovskite film, and surface passivation of pristine perovskite thin film using 3 μL CFBA treatment.

adsorbs on the perovskite surface via coulombic interaction (Pb-F) and hydrogen bonding (H-I). Fluoride ions (F^-) as associated with CFBA ionic molecule forms strong bonding with uncoordinated lead (Pb^{2+}) ions due to high electronegativity. The interaction of electron withdrawing -CF_3 functional group with uncoordinated Pb site is beneficial in many aspects such as to passivate uncoordinated surface Pb^{2+} ions, suppress halide ion vacancies, improve the hydrophobicity of perovskite surface. Thus, surface treatment with CFBA ionic liquid effectively reduced the pinholes, enhanced the crystallinity, improved surface coverage and compactness, inhibited surface defects, decreased trap-assisted charge carrier recombination, leading to higher photovoltaic performance, and better thermal stability. We believe that this study could offer a new pathway for further development of efficient and stable all-inorganic PSCs.

4. Conclusion

In summary, we demonstrated an effective approach to develop high-quality all-inorganic α-$CsPbI_2Br$ perovskite film under ambient conditions. The surface treatment of α-$CsPbI_2Br$ perovskite film with organic fluorinated CFBA molecule is benefited in multiple ways such as enhanced crystallinity, decreased pinholes, improved film coverage and compactness, passivated dangling bonds, produced dense morphology, prolong carrier lifetime, improved hydrophobicity, and remarkably reduced trap-assisted recombination, resulting in enhanced device PCE. Interestingly, the optimized CFBA concentration (3 μL) based device exhibited a noticeable PCE of 17.07%, which is higher than the pristine PSC (15.24%). Moreover, champion device maintained ~ 86.23% of its original PCE, whereas pristine PSC showed 48.26% retention of its initial PCE after monitoring 1400 h at 85 °C in dry box. In addition, we also examined indoor photovoltaic performance with and without CFBA treatment-based PSCs under LED lighting conditions (3200 K) at 1000 lx. As a result, indoor PCE related to pristine and 3 μL treated PSCs was found to be 23.24% and 18.35%, respectively. Notably, optimized PSC showed a high indoor PCE than pristine device, owing to formation of high-quality perovskite film after 3 μL CFBA modification. Our finding suggested that CFBA ionic liquid plays multi-functional roles to strongly mitigate the surface defects, leading to the high device PCE as well as remarkable stability. Therefore, present work provides a novel way to produce a high quality α-$CsPbI_2Br$ perovskite film, which will further promote the design of efficient and stable all-inorganic PSCs under outdoor/indoor lighting conditions.

CRediT authorship contribution statement

Jitendra Bahadur: Conceptualization, Methodology, Investigation, Validation, Data curation, Visualization, Formal analysis, Writing – original draft. **SungWon Cho:** Data curation, Visualization, Formal analysis. **Padmini Pandey:** Data curation, Investigation, Validation, Visualization, Formal analysis. **Jun Ryu:** Data curation, Visualization, Formal analysis. **Saemon Yoon:** Data curation, Visualization, Formal analysis. **Dong-Gun Lee:** Data curation, Visualization, Formal analysis. **Jun Tae Song:** Data curation, Visualization, Formal analysis. **Jung Sang Cho:** Conceptualization. **Dong-Won Kang:** Writing – review & editing, Conceptualization, Supervision, Project administration, Funding acquisition.

Declaration of Competing Interest

The authors declare that they have no known competing financial interests or personal relationships that could have appeared to influence the work reported in this paper.

Data availability

Data will be made available on request.

Acknowledgments

This work was supported by the National Research Foundation of Korea (NRF) grant funded by the Korea government (MSIT) (NRF - RS-2023-00212744, 2021R1A4A2001687, and 2021K2A9A2A08000082) and NRF- Brain Pool (Grant No.: 2022H1D3A2A01096254).

Appendix A. Supplementary material

Supplementary data to this article can be found online at https://doi.org/10.1016/j.apsusc.2023.157901.

References

[1] G. Li, J. Song, J. Wu, Z. Song, X. Wang, W. Sun, L. Fan, J. Lin, M. Huang, Z. Lan, Efficient and stable 2D@ 3D/2D perovskite solar cells based on dual optimization of grain boundary and interface, ACS Energy Lett. 6 (2021) 3614–3623.
[2] J. Sun, N. Chandrasekaran, C. Liu, A.D. Scully, W. Yin, C.K. Ng, J.J. Jasieniak, Enhancement of 3D/2D perovskite solar cells using an F4TCNQ molecular additive, ACS Appl. Energy Mater. 3 (2020) 8205–8215.
[3] W. Tang, Y. Chen, J. Yang, R. Yuan, Y. Lv, Q. Ma, Y. Wu, P. Zhang, W.-H. Zhang, Acetone-assisted precursor engineering enables low-temperature fabrication of CsPbI2Br perovskite for efficient solar cells, J. Power Sources 482 (2021), 228965.
[4] A. Kojima, K. Teshima, Y. Shirai, T. Miyasaka, Organometal halide perovskites as visible-light sensitizers for photovoltaic cells, J. Am. Chem. Soc. 131 (2009) 6050–6051.
[5] J. Park, J. Kim, H.-S. Yun, M.J. Paik, E. Noh, H.J. Mun, M.G. Kim, T.J. Shin, S. I. Seok, Controlled growth of perovskite layers with volatile alkylammonium chlorides, Nature 616 (2023) 724–730.
[6] F. Sahli, J. Werner, B.A. Kamino, M. Bräuninger, R. Monnard, B. Paviet-Salomon, L. Barraud, L. Ding, J.J. Diaz Leon, D. Sacchetto, Fully textured monolithic perovskite/silicon tandem solar cells with 25.2% power conversion efficiency, Nat. Mater. 17 (2018) 820–826.
[7] Z. Wang, L. Liu, X. Liu, D. Song, D. Shi, S. Wu, Y. Tong, H. Ren, M. Li, Y. Zheng, Uncovering synergistic effect of chloride additives for efficient quasi-2D perovskite solar cells, J. Chem. Eng. 432 (2022), 134367.
[8] S. Fu, W. Zhang, X. Li, L. Wan, Y. Wu, L. Chen, X. Liu, J. Fang, Dual-protection strategy for high-efficiency and stable CsPbI2Br inorganic perovskite solar cells, ACS Energy Lett. 5 (2020) 676–684.
[9] Q. Han, S. Yang, L. Wang, F. Yu, C. Zhang, M. Wu, T. Ma, The sulfur-rich small molecule boosts the efficiency of carbon-based $CsPbI_2Br$ perovskite solar cells to approaching 14%, Sol Energy 216 (2021) 351–357.
[10] L. Yu, T. Guo, H. Yuan, Z. Zhang, Z. Deng, R. Zhao, M. Zheng, J. Zhang, W. Xu, X. Liu, Effective lewis base additive with S-donor for efficient and stable $CsPbI_2Br$ based perovskite solar cells, J. Chem. Eng. 420 (2021), 129931.
[11] Y. Yang, M.T. Hoang, D. Yao, N.D. Pham, V.T. Tiong, X. Wang, H. Wang, Spiro-OMeTAD or CuSCN as a preferable hole transport material for carbon-based planar perovskite solar cells, J. Mater. Chem. A 8 (2020) 12723–12734.
[12] S. Yang, L. Wang, L. Gao, J. Cao, Q. Han, F. Yu, Y. Kamata, C. Zhang, M. Fan, G. Wei, Excellent moisture stability and efficiency of inverted all-inorganic CsPbIBr 2 perovskite solar cells through molecule interface engineering, ACS Appl. Mater. Interfaces 12 (2020) 13931–13940.
[13] S. Zheng, H. Wang, P. Wei, H. Chen, Y. Xie, Enhancing the performance and stability of carbon-based $CsPbI_2Br$ perovskite solar cells via tetrabutylammonium iodide surface passivation, Sol Energy 230 (2021) 666–674.
[14] M. Tai, Y. Zhou, X. Yin, J. Han, Q. Zhang, Y. Zhou, H. Lin, In situ formation of a 2D/3D heterostructure for efficient and stable $CsPbI_2Br$ solar cells, J. Mater. Chem. A 7 (2019) 22675–22682.
[15] R.J. Sutton, G.E. Eperon, L. Miranda, E.S. Parrott, B.A. Kamino, J.B. Patel, M. T. Hörantner, M.B. Johnston, A.A. Haghighirad, D.T. Moore, Bandgap-tunable cesium lead halide perovskites with high thermal stability for efficient solar cells, Adv. Energy Mater. 6 (2016) 1502458.
[16] J. Tian, Q. Xue, X. Tang, Y. Chen, N. Li, Z. Hu, T. Shi, X. Wang, F. Huang, C. J. Brabec, Dual interfacial design for efficient $CsPbI_2Br$ perovskite solar cells with improved photostability, Adv. Mater. 31 (2019) 1901152.
[17] H. Li, X. Hao, B. Chang, Z. Li, L. Wang, L. Pan, X. Chen, L. Yin, Stiffening the Pb-X Framework through a π-Conjugated Small-Molecule Cross-Linker for High-Performance Inorganic $CsPbI_2Br$ Perovskite Solar Cells, ACS Appl. Mater. Interfaces 13 (2021) 40489–40501.
[18] K. Jiang, J. Wang, F. Wu, Q. Xue, Q. Yao, J. Zhang, Y. Chen, G. Zhang, Z. Zhu, H. Yan, Dopant-free organic hole-transporting material for efficient and stable inverted all-inorganic and hybrid perovskite solar cells, Adv. Mater. 32 (2020) 1908011.
[19] X. Liu, H. Lian, Z. Zhou, C. Zou, J. Xie, F. Zhang, H. Yuan, S. Yang, Y. Hou, H. G. Yang, Stoichiometric dissolution of defective $CsPbI_2Br$ surfaces for inorganic solar cells with 17.5% efficiency, Adv. Energy Mater. 12 (2022) 2103933.
[20] W. Pan, J. Lin, J. Wu, X. Wang, G. Li, Y. Du, W. Li, W. Sun, Z. Lan, Efficient surface treatment based on an ionic imidazolium hexafluorophosphate for improving the efficiency and stability of perovskite solar cells, Appl. Surf. Sci. 604 (2022), 154486.
[21] B. Chen, P.N. Rudd, S. Yang, Y. Yuan, J. Huang, Imperfections and their passivation in halide perovskite solar cells, Chem. Soc. Rev. 48 (2019) 3842–3867.
[22] X. Zhu, M. Du, J. Feng, H. Wang, Z. Xu, L. Wang, S. Zuo, C. Wang, Z. Wang, C. Zhang, High-efficiency perovskite solar cells with imidazolium-based ionic liquid for surface passivation and charge transport, Angew. Chem., Int. Ed. 60 (2021) 4238–4244.
[23] H. Kim, S.U. Lee, D.Y. Lee, M.J. Paik, H. Na, J. Lee, S.I. Seok, Optimal interfacial engineering with different length of alkylammonium halide for efficient and stable perovskite solar cells, Adv. Energy Mater. 9 (2019) 1902740.
[24] M.K. Mohanta, A. Kishore, A. De Sarkar, Spin-current modulation in hexagonal buckled ZnTe and CdTe monolayers for self-powered flexible-piezo-spintronic devices, ACS Appl. Mater. Interfaces 13 (2021) 40872–40879.
[25] W. Chen, H. Chen, G. Xu, R. Xue, S. Wang, Y. Li, Y. Li, Precise control of crystal growth for highly efficient $CsPbI_2Br$ perovskite solar cells, Joule 3 (2019) 191–204.
[26] H. Zhao, Y. Han, Z. Xu, C. Duan, S. Yang, S. Yuan, Z. Yang, Z. Liu, S. Liu, A novel anion doping for stable $CsPbI_2Br$ perovskite solar cells with an efficiency of 15.56% and an open circuit voltage of 1.30 V, Adv. Energy Mater. 9 (2019) 1902279.
[27] H. Sun, J. Zhang, X. Gan, L. Yu, H. Yuan, M. Shang, C. Lu, D. Hou, Z. Hu, Y. Zhu, Pb-reduced $CsPb_{0.9}Zn_{0.1}I_2Br$ thin films for efficient perovskite solar cells, Adv. Energy Mater., 9 (2019) 1900896.
[28] S.S. Mali, J.V. Patil, J.A. Steele, S.R. Rondiya, N.Y. Dzade, C.K. Hong, Implementing dopant-free hole-transporting layers and metal-incorporated $CsPbI_2Br$ for stable all-inorganic perovskite solar cells, ACS Energy Lett. 6 (2021) 778–788.
[29] S.-C. Chen, D. Wang, Q. Zheng, Surface Passivation of All-Inorganic $CsPbI_2Br$ with a Fluorinated Organic Ammonium Salt for Perovskite Solar Cells with Efficiencies over 16%, Sol. RRL 4 (2020) 2000321.
[30] W. Zhang, S. Pathak, N. Sakai, T. Stergiopoulos, P.K. Nayak, N.K. Noel, A. A. Haghighirad, V.M. Burlakov, D.W. Dequilettes, A. Sadhanala, Enhanced optoelectronic quality of perovskite thin films with hypophosphorous acid for planar heterojunction solar cells, Nat. Commun. 6 (2015) 10030.
[31] Y. Deng, X. Li, R. Wang, Carboxyl functional group-assisted defects passivation strategy for efficient air-processed perovskite solar cells with excellent ambient stability, Sol. Energy Mater. Sol. Cells 230 (2021), 111242.
[32] X. Liu, J. Wu, Y. Yang, D. Wang, G. Li, X. Wang, W. Sun, Y. Wei, Y. Huang, M. Huang, Additive engineering by bifunctional guanidine sulfamate for highly efficient and stable perovskites solar cells, Small 16 (2020) 2004877.
[33] Y. Du, J. Wu, X. Zhang, Q. Zhu, M. Zhang, X. Liu, Y. Zou, S. Wang, W. Sun, Surface passivation using pyridinium iodide for highly efficient planar perovskite solar cells, J. Energy Chem. 52 (2021) 84–91.
[34] C. Qin, T. Matsushima, T. Fujihara, C. Adachi, Multifunctional benzoquinone additive for efficient and stable planar perovskite solar cells, Adv. Mater. 29 (2017) 1603808.
[35] X. Zhang, D. Zhang, T. Guo, C. Zheng, Y. Zhou, J. Jin, Z. Zhu, Z. Wang, X. Cui, S. Wu, The synergistic effect of defect passivation and energy level adjustment for low-temperature carbon-based $CsPbI_2Br$ perovskite solar cells, J. Mater. Chem. C 10 (2022) 15573–15581.
[36] X.-N. Huo, K.-X. Wang, R. Yin, W.-W. Sun, Y.-S. Sun, Y.-K. Gao, T.-T. You, P.-G. Yin, High-performance carbon-based all-inorganic $CsPbI_2Br$ perovskite solar cells via ethylammonium iodide and phenethylammonium iodide synergistic passivation, Sol. Energy Mater. Sol. Cells 247 (2022), 111963.
[37] J. He, J. Su, Z. Lin, J. Ma, L. Zhou, S. Zhang, S. Liu, J. Chang, Y. Hao, Enhanced efficiency and stability of all-inorganic $CsPbI_2Br$ perovskite solar cells by organic and ionic mixed passivation, Adv. Sci. 8 (2021) 2101367.
[38] W.-Q. Wu, P.N. Rudd, Z. Ni, C.H. Van Brackle, H. Wei, Q. Wang, B.R. Ecker, Y. Gao, J. Huang, Reducing surface halide deficiency for efficient and stable iodide-based perovskite solar cells, J. Am. Chem. Soc. 142 (2020) 3989–3996.
[39] Y. Zhang, C. Wu, D. Wang, Z. Zhang, X. Qi, N. Zhu, G. Liu, X. Li, H. Hu, Z. Chen, High efficiency (16.37%) of cesium bromide—passivated all-inorganic $CsPbI_2Br$ perovskite solar cells, Sol. RRL 3 (2019) 1900254.
[40] Q. Jiang, D. Rebollar, J. Gong, E.L. Piacentino, C. Zheng, T. Xu, Pseudohalide-induced moisture tolerance in perovskite $CH_3NH_3Pb(SCN)_2I$ thin films, Angew. Chem. 127 (2015) 7727–7730.
[41] J. Chen, S.G. Kim, N.G. Park, $FA_{0.88}Cs_{0.12}PbI_{3-x}(PF_6)_x$ interlayer formed by ion exchange reaction between perovskite and hole transporting layer for improving photovoltaic performance and stability, Adv. Mater. 30 (2018) 1801948.
[42] J. Zhang, S. Wu, T. Liu, Z. Zhu, A.K.Y. Jen, Boosting photovoltaic performance for lead halide perovskites solar cells with BF_4^- anion substitutions, Adv. Funct. Mater. 29 (2019) 1808833.
[43] J. Xu, J. Cui, S. Yang, Y. Han, X. Guo, Y. Che, D. Xu, C. Duan, W. Zhao, K. Guo, Unraveling passivation mechanism of imidazolium-based ionic liquids on inorganic perovskite to achieve near-record-efficiency $CsPbI_2Br$ solar cells, Nanomicro Lett. 14 (2022) 7.
[44] A. Wang, X. Deng, J. Wang, S. Wang, X. Niu, F. Hao, L. Ding, Ionic liquid reducing energy loss and stabilizing $CsPbI_2Br$ solar cells, Nano Energy 81 (2021), 105631.
[45] M. Shahiduzzaman, E.Y. Muslih, A.M. Hasan, L. Wang, S. Fukaya, M. Nakano, M. Karakawa, K. Takahashi, M. Akhtaruzzaman, J.-M. Nunzi, The benefits of ionic liquids for the fabrication of efficient and stable perovskite photovoltaics, J. Chem. Eng. 411 (2021), 128461.
[46] J. Luo, F. Lin, J. Yuan, Z. Wan, C. Jia, Application of ionic liquids and derived materials to high-efficiency and stable perovskite solar cells, ACS Materials Letters 4 (2022) 1684–1715.

[47] D. Yang, R. Yang, X. Ren, X. Zhu, Z. Yang, C. Li, S. Liu, Hysteresis-suppressed high-efficiency flexible perovskite solar cells using solid-state ionic-liquids for effective electron transport, Adv. Mater. 28 (2016) 5206–5213.

[48] X. Pu, J. Han, S. Wang, H. Zhou, Q. Cao, J. Yang, Z. He, X. Li, Surface modification with ionic liquid for efficient $CsPbI_2Br$ perovskite solar cells, J Materiomics. 7 (2021) 1039–1048.

[49] Y. Wu, W. Zhao, W. Wang, W. Sui, Fabricating binary anti-corrosion structures containing superhydrophobic surfaces and sturdy barrier layers for Al alloys, RSC Adv. 6 (2016) 5100–5110.

[50] K. Wei, L. Yang, J. Deng, Z. Luo, X. Zhang, J. Zhang, Facile Exfoliation of the Perovskite Thin Film for Visualizing the Buried Interfaces in Perovskite Solar Cells, ACS Appl. Energy Mater. 5 (2022) 7458–7465.

[51] N. Celebi, M.Y. Aydin, F. Soysal, N. Yıldız, K. Salimi, Core/shell PDA@ UiO-66 metal–organic framework nanoparticles for efficient visible-light photodegradation of organic dyes, ACS Appl. Nano Mater. 3 (2020) 11543–11554.

[52] K.H. Wang, L. Wang, Y.Y. Liu, Y.H. Song, Y.C. Yin, J.S. Yao, J.N. Yang, J.J. Wang, L.Z. Feng, Q. Zhang, High quality $CsPbI_{3-}$ xB_rx thin films enabled by synergetic regulation of fluorine polymers and amino acid molecules for efficient pure red light emitting diodes, Advanced Optical Materials 9 (2021) 2001684.

[53] J. Wang, L. Chen, Z. Qian, G. Ren, J. Wu, H. Zhang, Optimal intermediate adducts regulate low-temperature $CsPbI_2Br$ crystallization for efficient inverted all-inorganic perovskite solar cells, J. Mater. Chem. A 8 (2020) 25336–25344.

[54] X. Yang, J. Han, W. Ruan, Y. Hu, Z. He, X. Jia, S. Zhang, D. Wang, Low temperature fabrication for high-performance semitransparent $CsPbI_2Br$ perovskite solar cells, Chin. Chem. Lett. 33 (2022) 1425–1429.

[55] J. Zhuang, Y. Wei, Y. Luan, N. Chen, P. Mao, S. Cao, J. Wang, Band engineering at the interface of all-inorganic $CsPbI_2Br$ solar cells, Nanoscale 11 (2019) 14553–14560.

[56] K. Zheng, C. Liu, K. Yu, Y. Meng, X. Yin, S. Bu, B. Han, C. Liu, Z. Ge, Interfacial engineering strategy based on polymer modification to regulate the residual stress in $CsPbI_2Br$ based perovskite solar cells, J. Chem. Eng. 446 (2022), 137307.

[57] W. Feng, Y. Tan, M. Yang, Y. Jiang, B.-X. Lei, L. Wang, W.-Q. Wu, Small amines bring big benefits to perovskite-based solar cells and light-emitting diodes, Chem 8 (2022) 351–383.

[58] H. Chen, Y. Ma, X. Wang, G. Yao, Y. Du, J. Zhou, L. Zhu, X. Zhao, S. Yang, X. Liu, Improving the stability and efficiency of inorganic $CsPbI_2Br$ perovskite via surface reconstruction strategy, J. Chem. Eng. 442 (2022), 136242.

[59] J. Bahadur, J. Ryu, P. Pandey, S. Cho, J.S. Cho, D.-W. Kang, In situ crystal reconstruction strategy-based highly efficient air-processed inorganic $CsPbI_2Br$ perovskite photovoltaics for indoor, outdoor, and switching applications, Nanoscale 15 (2023) 3850–3863.

[60] D. Bai, J. Zhang, Z. Jin, H. Bian, K. Wang, H. Wang, L. Liang, Q. Wang, S.F. Liu, Interstitial Mn^{2+}-driven high-aspect-ratio grain growth for low-trap-density microcrystalline films for record efficiency $CsPbI_2Br$ solar cells, ACS Energy Lett. 3 (2018) 970–978.

[61] S. Khalid, M.A. Malik, D.J. Lewis, P. Kevin, E. Ahmed, Y. Khan, P. O'Brien, Transition metal doped pyrite (FeS_2) thin films: structural properties and evaluation of optical band gap energies, J. Mater. Chem. C 3 (2015) 12068–12076.

[62] J. Bahadur, J. Ryu, D.-G. Lee, J. Hong, S. Hayase, J.S. Cho, S.M. Jeong, D.-W. Kang, In-situ surface defects passivation with small carbon chain molecules for highly efficient, air-processed inorganic $CsPbI_2Br$ perovskite photovoltaics, Appl. Surf. Sci. 614 (2023), 156229.

[63] V. Mote, Y. Purushotham, B. Dole, Williamson-Hall analysis in estimation of lattice strain in nanometer-sized ZnO particles, J. Theor. Appl. Phys. 6 (2012) 1–8.

[64] P. Chelvanathan, Y. Yusoff, F. Haque, M. Akhtaruzzaman, M. Alam, Z. Alothman, M. Rashid, K. Sopian, N. Amin, Growth and characterization of RF-sputtered ZnS thin film deposited at various substrate temperatures for photovoltaic application, Appl. Surf. Sci. 334 (2015) 138–144.

[65] Y. Kumar, E. Regalado-Pérez, A.M. Ayala, N. Mathews, X. Mathew, Effect of heat treatment on the electrical properties of perovskite solar cells, Sol. Energy Mater. Sol. Cells 157 (2016) 10–17.

[66] J.V. Patil, S.S. Mali, C.K. Hong, Reducing Defects of All-Inorganic γ-$CsPbI_2Br$ Thin Films by Ethylammonium Bromide Additives for Efficient Perovskite Solar Cells, ACS Appl. Mater. Interfaces 14 (2022) 25576–25583.

[67] J.V. Patil, S.S. Mali, C.K. Hong, Grain size enlargement and controlled crystal growth by formamidinium chloride additive-added γ-$CsPbI_2Br$ thin films for stable inorganic perovskite solar cells, Mater. Today Chem. 26 (2022), 101118.

[68] K.S. Kim, I.S. Jin, S.H. Park, S.J. Lim, J.W. Jung, Methylammonium iodide-mediated controlled crystal growth of $CsPbI_2Br$ films for efficient and stable all-inorganic perovskite solar cells, ACS Appl. Mater. Interfaces 12 (2020) 36228–36236.

[69] S. Fu, J. Wang, X. Liu, H. Yuan, Z. Xu, Y. Long, J. Zhang, L. Huang, Z. Hu, Y. Zhu, Multifunctional liquid additive strategy for highly efficient and stable $CsPbI_2Br$ all-inorganic perovskite solar cells, J. Chem. Eng. 422 (2021), 130572.

[70] X. Li, C.C. Chen, M. Cai, X. Hua, F. Xie, X. Liu, J. Hua, Y.T. Long, H. Tian, L. Han, Efficient Passivation of Hybrid Perovskite Solar Cells Using Organic Dyes with -COOH Functional Group, Adv. Energy Mater. 8 (2018) 1800715.

[71] S. Fu, X. Li, L. Wan, Y. Wu, W. Zhang, Y. Wang, Q. Bao, J. Fang, Efficient passivation with lead pyridine-2-carboxylic for high-performance and stable perovskite solar cells, Adv. Energy Mater. 9 (2019) 1901852.

[72] Z. Zeng, J. Zhang, X. Gan, H. Sun, M. Shang, D. Hou, C. Lu, R. Chen, Y. Zhu, L. Han, In situ grain boundary functionalization for stable and efficient inorganic $CsPbI_2Br$ perovskite solar cells, Adv. Energy Mater. 8 (2018) 1801050.

[73] K. Nishimura, M.A. Kamarudin, D. Hirotani, K. Hamada, Q. Shen, S. Iikubo, T. Minemoto, K. Yoshino, S. Hayase, Lead-free tin-halide perovskite solar cells with 13% efficiency, Nano Energy 74 (2020), 104858.

[74] W. Qi, J. Li, Y. Li, K. Sohail, H. Ling, P. Wang, S. Jiao, F. Liu, X. Zhou, H. Wang, Manipulated crystallization and passivated defects for efficient perovskite solar cells via addition of ammonium iodide, ACS Appl. Mater. Interfaces 13 (2021) 34053–34063.

[75] Z. Zhang, M.A. Kamarudin, A.K. Baranwal, L. Wang, G. Kapil, S.R. Sahamir, Y. Sanehira, M. Chen, Q. Shen, S. Hayase, Indent-Free Vapor-Assisted Surface Passivation Strategy toward Tin Halide Perovskite Solar Cells, ACS Appl. Mater. Interfaces 14 (2022) 36200–36208.

[76] K.-L. Wang, R. Wang, Z.-K. Wang, M. Li, Y. Zhang, H. Ma, L.-S. Liao, Y. Yang, Tailored phase transformation of $CsPbI_2Br$ films by copper (II) bromide for high-performance all-inorganic perovskite solar cells, Nano Lett. 19 (2019) 5176–5184.

[77] H. Li, L. Yin, Efficient Bidentate Molecules Passivation Strategy for High-Performance and Stable Inorganic $CsPbI_2Br$ Perovskite Solar Cells, Sol. RRL 4 (2020) 2000268.

[78] Y. Jiang, Z. Lu, S. Zou, H. Lai, Z. Zhang, J. Luo, Y. Huang, R. He, J. Jin, Z. Yi, Dual-site passivation of tin-related defects enabling efficient lead-free tin perovskite solar cells, Nano Energy 103 (2022), 107818.

[79] M. Grischek, P. Caprioglio, J. Zhang, F. Pena-Camargo, K. Sveinbjörnsson, F. Zu, D. Menzel, J.H. Warby, J. Li, N. Koch, Efficiency Potential and Voltage Loss of Inorganic $CsPbI_2Br$ Perovskite Solar Cells, Sol. RRL 6 (2022) 2200690.

[80] Z. Liu, S. Wu, X. Yang, Y. Zhou, J. Jin, J. Sun, L. Zhao, S. Wang, The dual interfacial modification of 2D gC_3N_4 for high-efficiency and stable planar perovskite solar cells, Nanoscale Adv. 2 (2020) 5396–5402.

[81] J.V. Patil, S.S. Mali, C.K. Hong, A-site rubidium cation-incorporated $CsPbI_2Br$ all-inorganic perovskite solar cells exceeding 17% efficiency, Sol. RRL 4 (2020) 2000164.

[82] Y.C. Wang, J. Chang, L. Zhu, X. Li, C. Song, J. Fang, Electron-transport-layer-assisted crystallization of perovskite films for high-efficiency planar heterojunction solar cells, Adv. Funct. Mater. 28 (2018) 1706317.

[83] G. Niu, W. Li, F. Meng, L. Wang, H. Dong, Y. Qiu, Study on the stability of $CH_3NH_3PbI_3$ films and the effect of post-modification by aluminum oxide in all-solid-state hybrid solar cells, J. Mater. Chem. A 2 (2014) 705–710.

[84] A. Guerrero, J. Bisquert, G. Garcia-Belmonte, Impedance spectroscopy of metal halide perovskite solar cells from the perspective of equivalent circuits, Chem. Rev. 121 (2021) 14430–14484.

[85] Y. Yang, J. Song, Y. Zhao, L. Zhu, X. Gu, Y. Gu, M. Che, Y. Qiang, Ammonium-iodide-salt additives induced photovoltaic performance enhancement in one-step solution process for perovskite solar cells, J. Alloys Compd. 684 (2016) 84–90.

[86] J. Song, S. Li, Y. Zhao, J. Yuan, Y. Zhu, Y. Fang, L. Zhu, X. Gu, Y. Qiang, Performance enhancement of perovskite solar cells by doping TiO2 blocking layer with group VB elements, J. Alloys Compd. 694 (2017) 1232–1238.

[87] F. Yang, D. Hirotani, G. Kapil, M.A. Kamarudin, C.H. Ng, Y. Zhang, Q. Shen, S. Hayase, All-Inorganic $CsPb_{1-x}Ge_xI_2Br$ Perovskite with Enhanced Phase Stability and Photovoltaic Performance, Angew. Chem. 130 (2018) 12927–12931.

[88] M. Li, F. Igbari, Z.K. Wang, L.S. Liao, Indoor thin-film photovoltaics: progress and challenges, Adv. Energy Mater. 10 (2020) 2000641.

[89] I. Mathews, S.N.R. Kantareddy, S. Sun, M. Layurova, J. Thapa, J.P. Correa-Baena, R. Bhattacharyya, T. Buonassisi, S. Sarma, I.M. Peters, Self-powered sensors enabled by wide-bandgap perovskite indoor photovoltaic cells, Adv. Funct. Mater. 29 (2019) 1904072.

[90] K.-L. Wang, Y.-H. Zhou, Y.-H. Lou, Z.-K. Wang, Perovskite indoor photovoltaics: Opportunity and challenges, Chemical Science 12 (2021) 11936–11954.

[91] A.S. Teran, J. Wong, W. Lim, G. Kim, Y. Lee, D. Blaauw, J.D. Phillips, AlGaAs photovoltaics for indoor energy harvesting in mm-scale wireless sensor nodes, IEEE Trans. Electron Dev. 62 (2015) 2170–2175.

[92] V. Pecunia, L.G. Occhipinti, R.L. Hoye, Emerging indoor photovoltaic technologies for sustainable internet of things, Adv. Energy Mater. 11 (2021) 2100698.

[93] V. Annapureddy, H. Palneedi, G.-T. Hwang, M. Peddigari, D.-Y. Jeong, W.-H. Yoon, K.-H. Kim, J. Ryu, Magnetic energy harvesting with magnetoelectrics: an emerging technology for self-powered autonomous systems, Sustain Energy Fuels 1 (2017) 2039–2052.

[94] M.T. Todaro, F. Guido, L. Algieri, V.M. Mastronardi, D. Desmaële, G. Epifani, M. De Vittorio, Biocompatible, flexible, and compliant energy harvesters based on piezoelectric thin films, IEEE Trans. Nanotechnol 17 (2018) 220–230.

[95] L. Zhou, J. Su, Z. Lin, X. Guo, J. Ma, T. Li, J. Zhang, J. Chang, Y. Hao, Synergistic interface layer optimization and surface passivation with fluorocarbon molecules toward efficient and stable inverted planar perovskite solar cells, Res. 2021 (2021).